Supplementary information

A universal graphitic interlayered centroid intercalation theory for intercalation chemistry

Kemeng Ji, et al.

*Email address: kmji@tju.edu.cn (K.M.J.)

Tianjin University, Tianjin, 300350, P. R. China.

Supplementary Figures

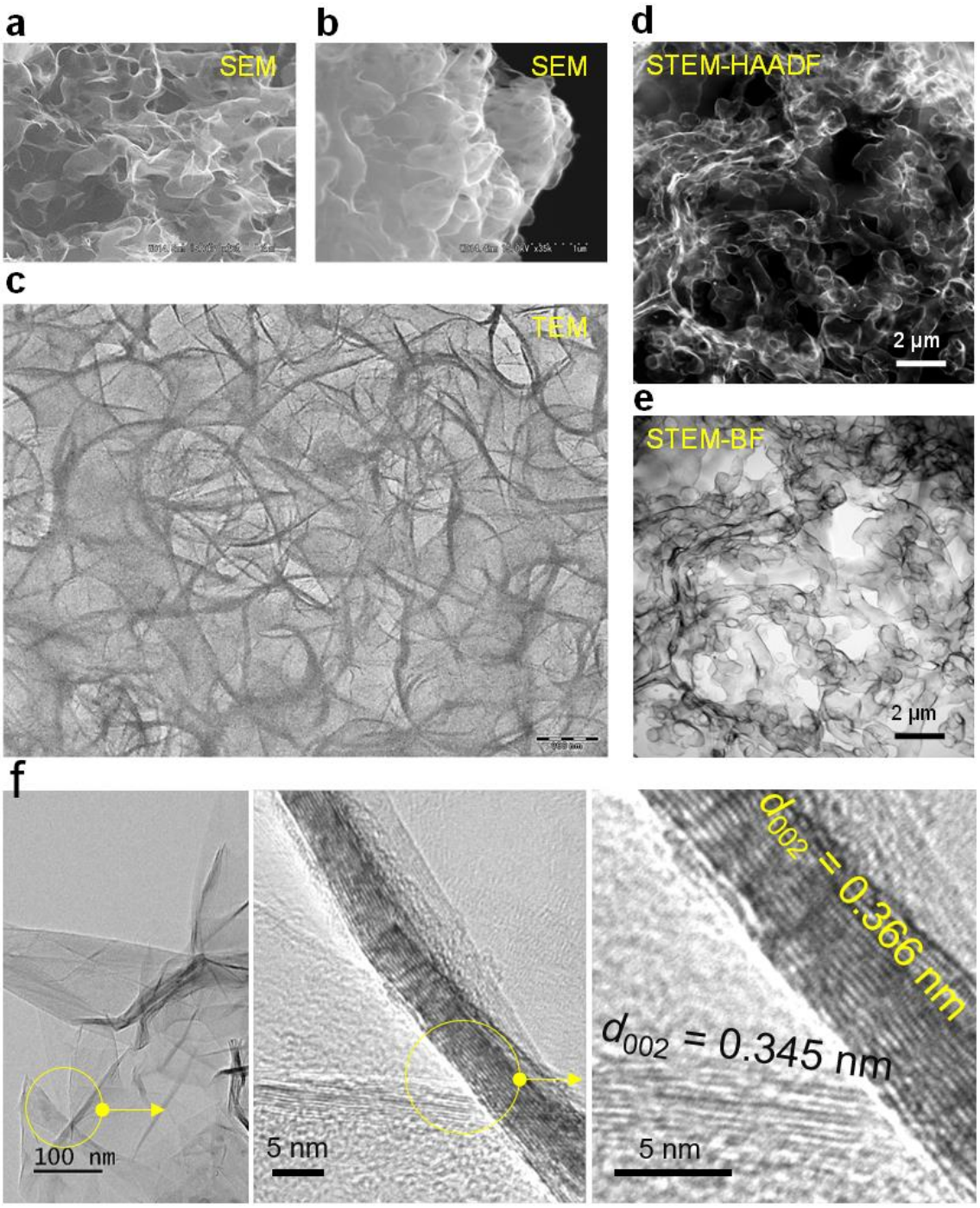

Supplementary Fig. 1 | Electron microscopy images of the typical NGF material. a, b, SEM images. **c, f,** TEM and HR-TEM images. **d, e,** HAADF- and BF-STEM images. The diameters for the Ni@graphene ligaments are mainly ranged at 300–500 nm. Few Ni particles are observed, in line with the following XPS and EDS results for its residual amounts (Supplementary Fig. 2). The d_{002} spacings observed from the edge planes are varied from 0.34 nm to 0.37 nm.

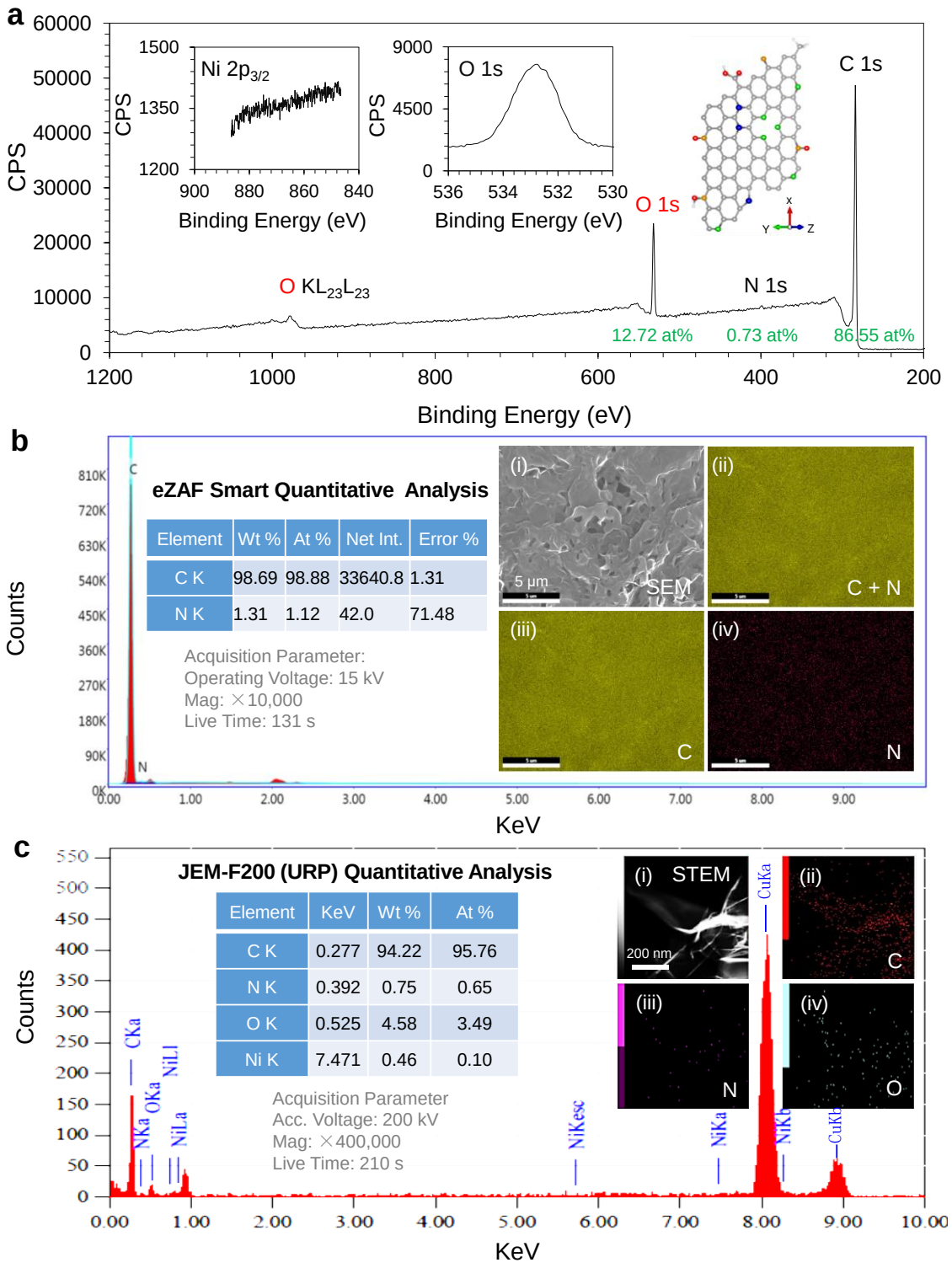

Supplementary Fig. 2 | Chemical position analysis for the typical NGF material. a, Full, Ni, and O 1s XPS spectra. The inset illustrates the different N species and some possible dangling functional groups at the edge of a single graphene sheet. **b, c,** EDS mapping images and relative contents for various possible elements. Only trace amounts of Ni were detected. The content of doped N element was less than 1 at%.

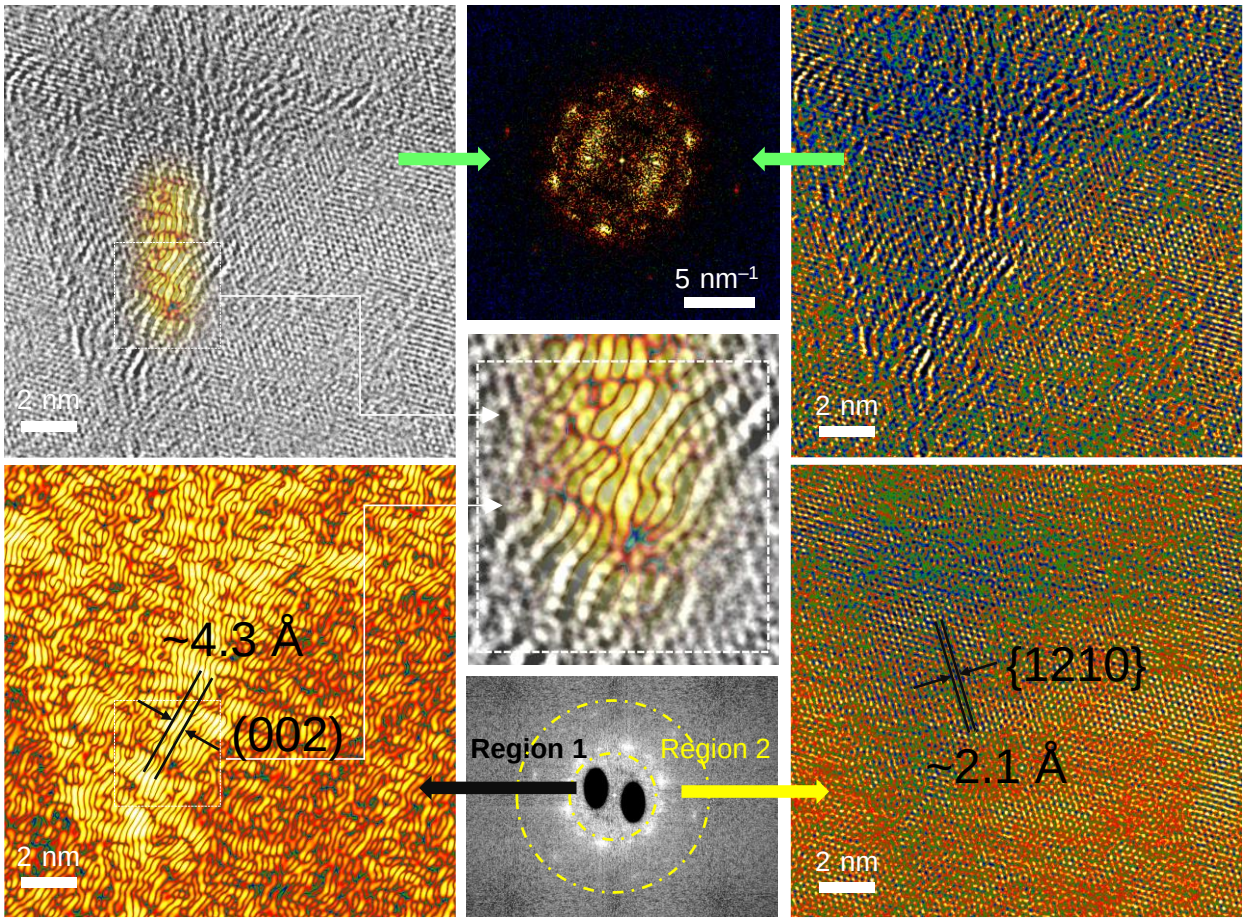

Supplementary Fig. 3 | A typical HR-TEM image for defective area of the NGF material, as well as its FFT pattern and FFT image rendered in color. The FFT diffraction pattern with a non-orthohexagonal or oblong shape implies that this defective region should come from the curved or bended part of the foam[1]. Because different diffraction spots are assigned to different crystal planes, it is possible to use this image and the mask tool in the DigitalMicrograph software to obtain the specific image of a particular crystal face, as illustrated by the colored images.

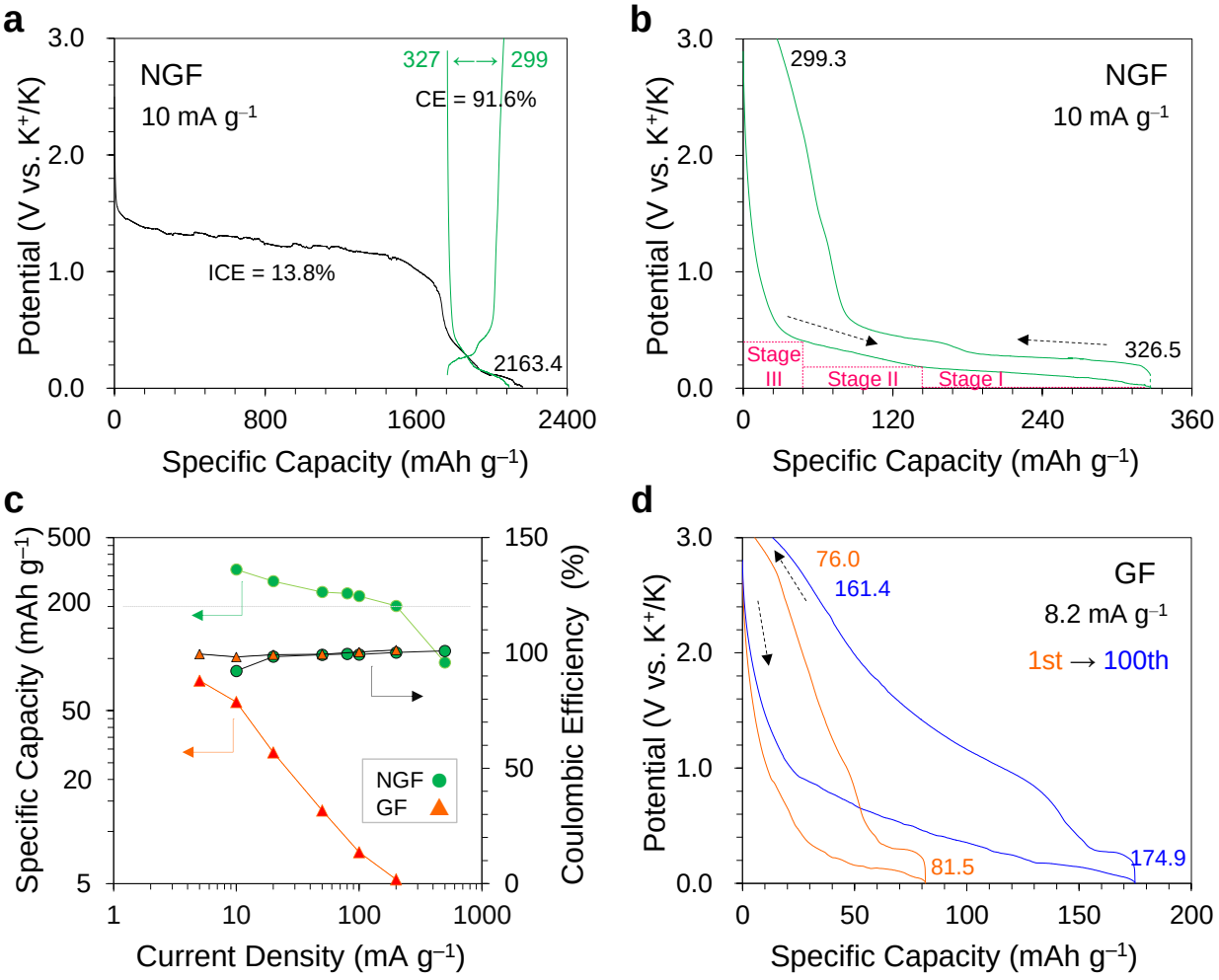

Supplementary Fig. 4 | Typical GCD curves and comparative rate performances of NGF and GF. a, b, Initial discharged curve (black line) of NGF (**a**) and its typical CD curves (**b**) at 10 mA g^{-1}. After the SEI formation at the potential range of 1.0–1.4 V during the 1st discharging process, its discharged and charged capacities generally remained at 326 and 299 mAh g^{-1}, respectively. **c,** Rate performances in capacity based on the data in Fig. 2 a, b. **d,** The CD curves of the GF sample before and after cycling at 8.2 mA g^{-1} for 100 cycles (refer to Fig. 2d).

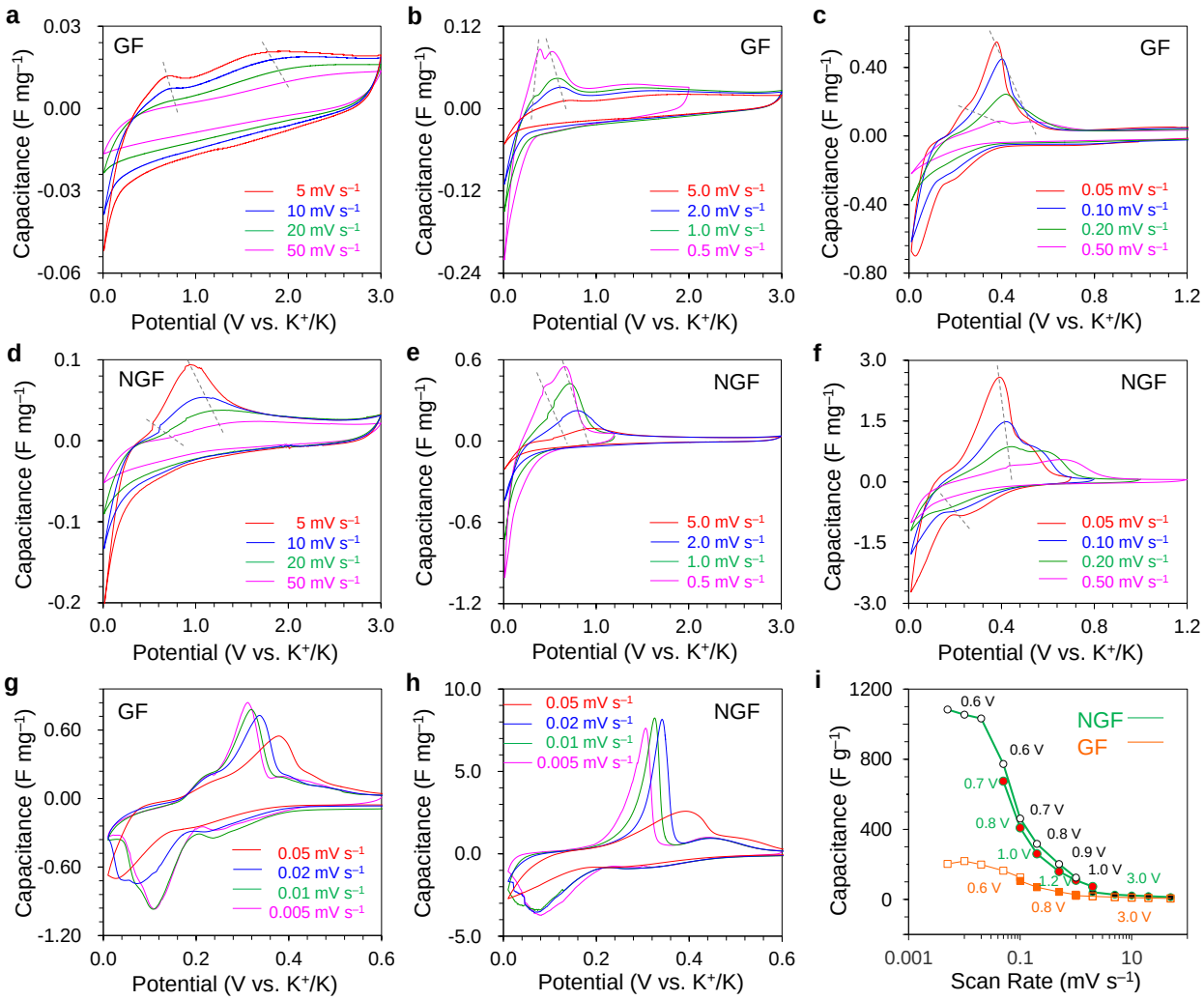

Supplementary Fig. 5 | Comparative CV curves and specific capacitances of the NGF and GF at varied scan rates from 50 mV s^{-1} to 0.005 mV s^{-1}. a–c, g, CV curves of GF. **d–f, h,** CV curves of NGF. **i,** Comparative rate performances in capacitance of the two materials at different CV scan rates and working potential regions. The high-end cut-off potentials used for the calculations (namely the numbers marked in the figure) were determined one by one according to the specific CV curves obtained at each scan rate, as shown in (**a–h**).

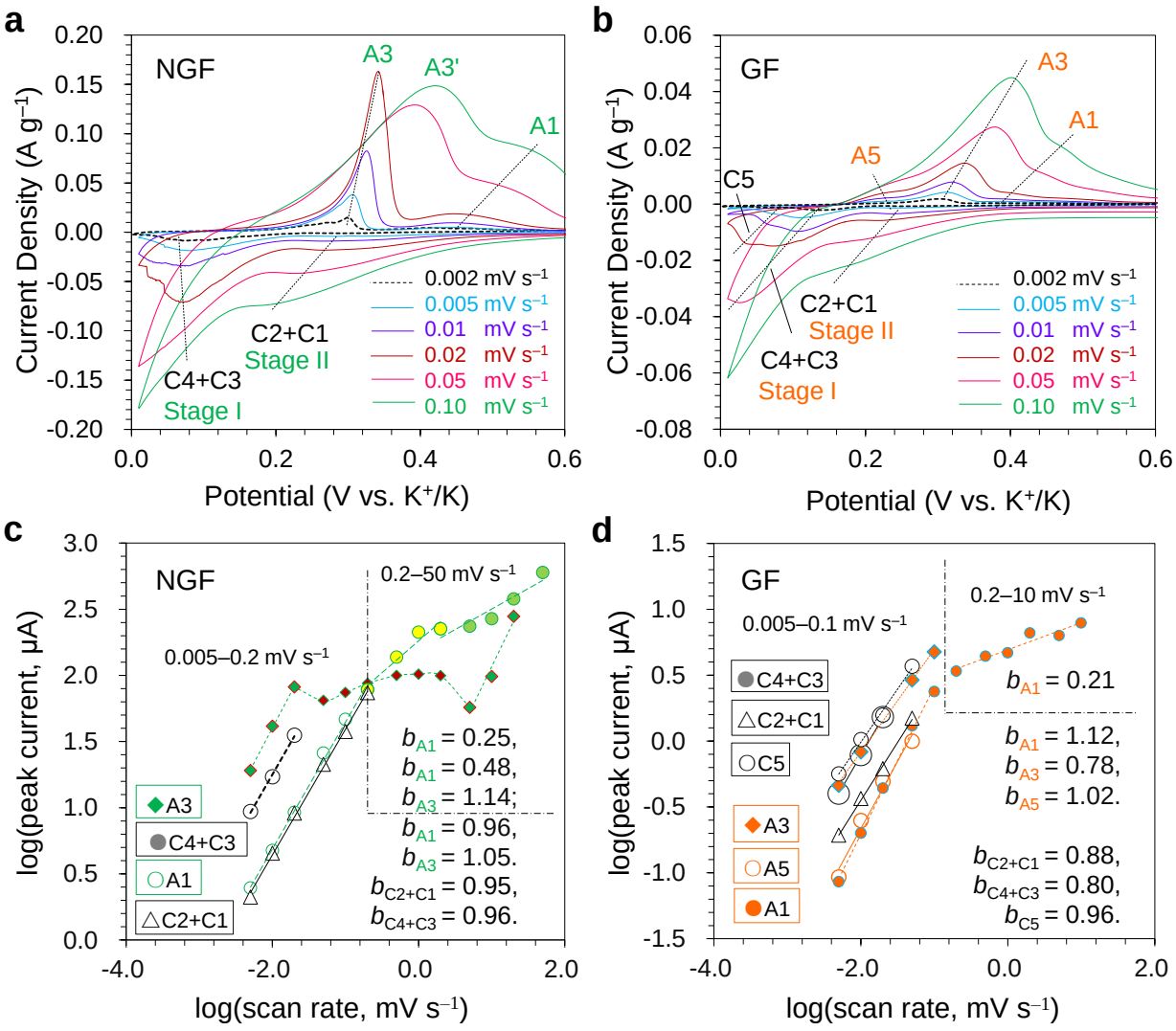

Supplementary Fig. 6 | CV curves of the freestanding NGF and GF electrodes at 0.10 to 0.002 mV s^{-1} and kinetics analysis of the *b* values based on the cathodic and anodic peak currents. **a, b,** CV curves of NGF (**a**) and GF (**b**). The CV peaks at Stage I and Stage II would split into two peaks at slow enough scan rates (e.g., ≤ 0.02 mV s^{-1}), implying the formation of two metastable mesophases at either stage (refer to Supplementary Fig. 7a, b). However, because of the high overlap of C1 and C2 peaks at Stage II as well as C3 and C4 peaks at Stage I, they are still regarded as one to calculate the *b* values as shown in (**c**, **d**). **c, d,** Kinetics analysis of the *b* values at different CV scan rates for NGF (**c**) and GF (**d**). Judging from the obtained *b* values, which are generally between 0.5 and 1.0, there may appear a relatively large error in the calculation when the scan rates are higher than 0.2 mV s^{-1}. Hence, the results obtained over 0.2 mV s^{-1} are just a reference for evaluating the dynamics.

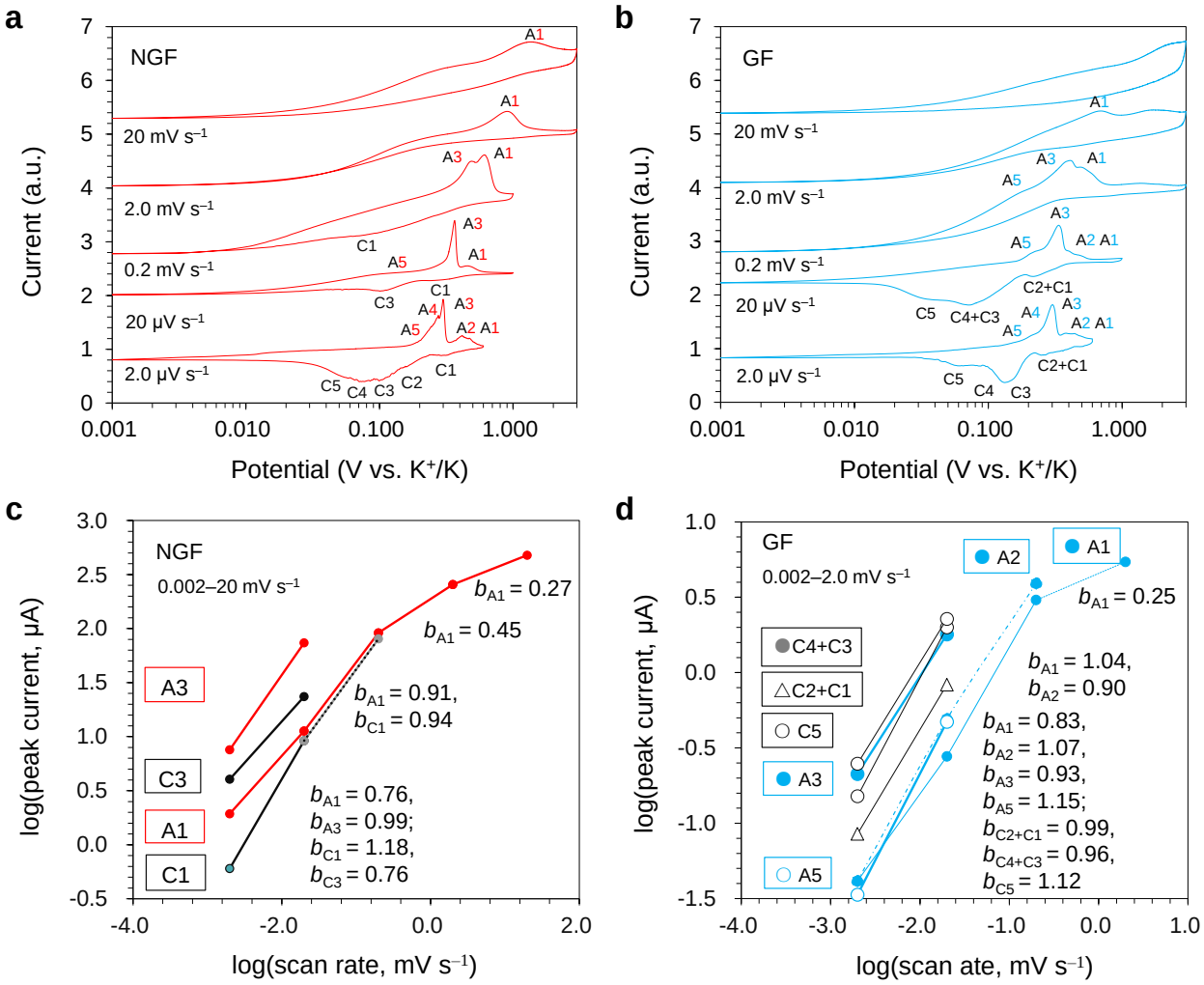

Supplementary Fig. 7 | Comparative CV curves of the freestanding NGF and GF electrodes at scan rates varied from 20 to 2.0, 0.2, 0.02, and 0.002 mV s^{-1} and the corresponding *b* values corresponding to every scan-rate range. a, b, CV curves of NGF (**a**) and GF (**b**), which clearly display the shape evolution of the CV curves as a function of scan rate. **c, d,** Kinetics analysis of the *b* values based on the CV peaks marked in (**a**, **b**) for NGF (**c**) and GF (**d**). Since few data points were collected here, the *b* values provided here were only as reference for the results in Supplementary Fig. 6.

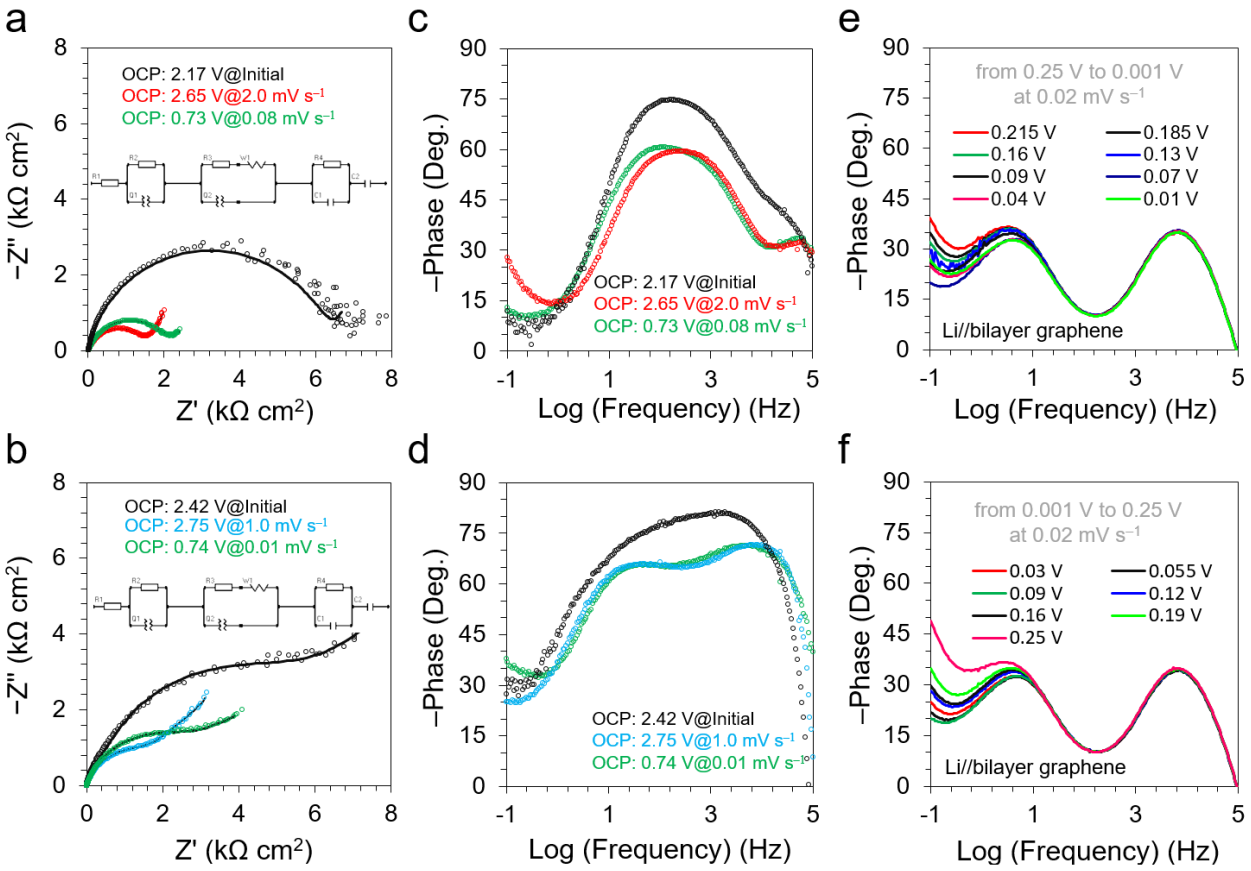

Supplementary Fig. 8 | Nyquist plots and Bode diagrams for various graphene foam electrode materials. a, b, Experimental and simulative (the solid lines) Nyquist plots or AC electrochemical impedance spectra (EIS) for the potassiated NGF (**a**) and GF (**b**) samples at different states (at the very beginning and after the CV tests at various scan rates). The inset refers to the equivalent circuit to simulate the Nyquist plots here[1]. The numbers before the @ symbol refer to the open-circuit potentials (OCPs) before the EIS measurements. **c–f,** Bode diagrams for the potassiated NGF (**c**) and GF (**d**) as well as the lithiated bilayer graphene samples (**e, f**) we previously reported (refer to **Supplementary Fig. 10** in ref. 1). The phase degree at 45° generally implies an ion-solid-diffusion controlled process, while a vale at 90° refers to a purely capacitive reaction[2]. As a result, from a kinetic point of view, potassium ions seem to diffuse more easily in graphene interlayers than lithium ions. The possible reason is that potassium has a larger atom diameter than lithium (4.54 Å vs. 3.04 Å), so that it can spread graphene interlayer spacing much larger to facilitate the diffusion of K ions (2.76 Å vs. 1.52 Å of Li^+) in the interlayer.

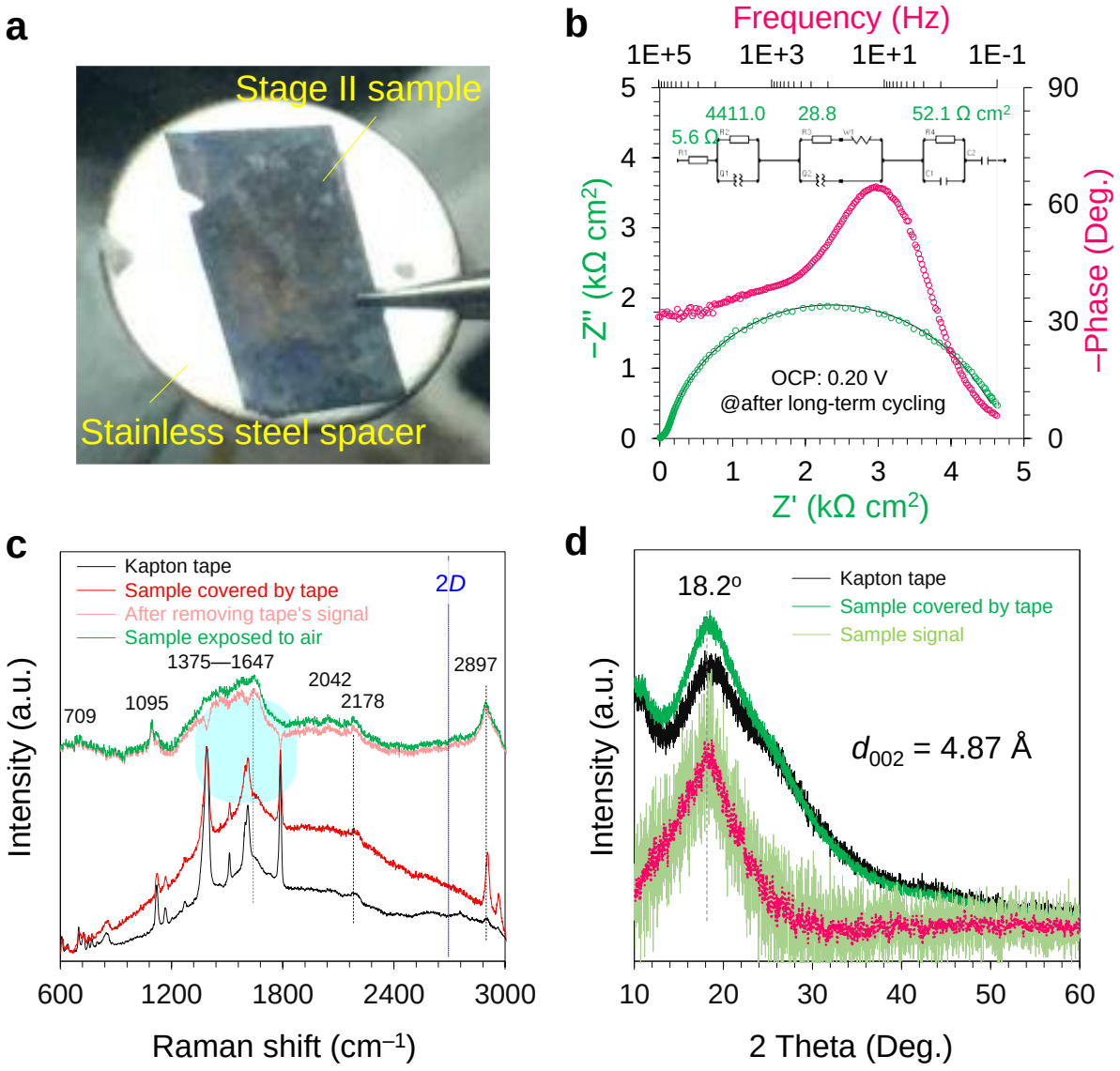

Supplementary Fig. 9 | Physiochemical characterizations for the Stage-II potassiated NGF sample. a, Optical photograph of the sample after a long-term cycling test as shown in Fig. 2c. **b,** Nyquist plot and Bode diagram of the sample after fully potassiation at 0.20 V and before disassembling the coin cell. **c,** Raman spectra of the sample (before and after being exposed in air) and the Kapton tape (applied to protect the sample from being oxidized in air). Due to the intercalation of K atoms into the graphene interlayer as well as its great influence on the honeycomb lattice, the 2*D* band originating from a second-order double-resonant Raman scattering mechanism disappeared. Instead, the bands between *D* and *G* bands enhanced a lot and a typical band characterized of C–H bonds appeared at 2897 cm^{-1}. Such results should prove the strong interaction between the intercalated K atoms and carbon planes. **d,** XRD patterns of the sample and the Kapton tape covered on its surface for the test. According to the (002) diffraction angle, the d_{002} interlayer spacing was estimated to be centered at 4.87 Å, a little larger than the widely reported value of the Stage-II K-GICS (~4.39 Å)[3,4].

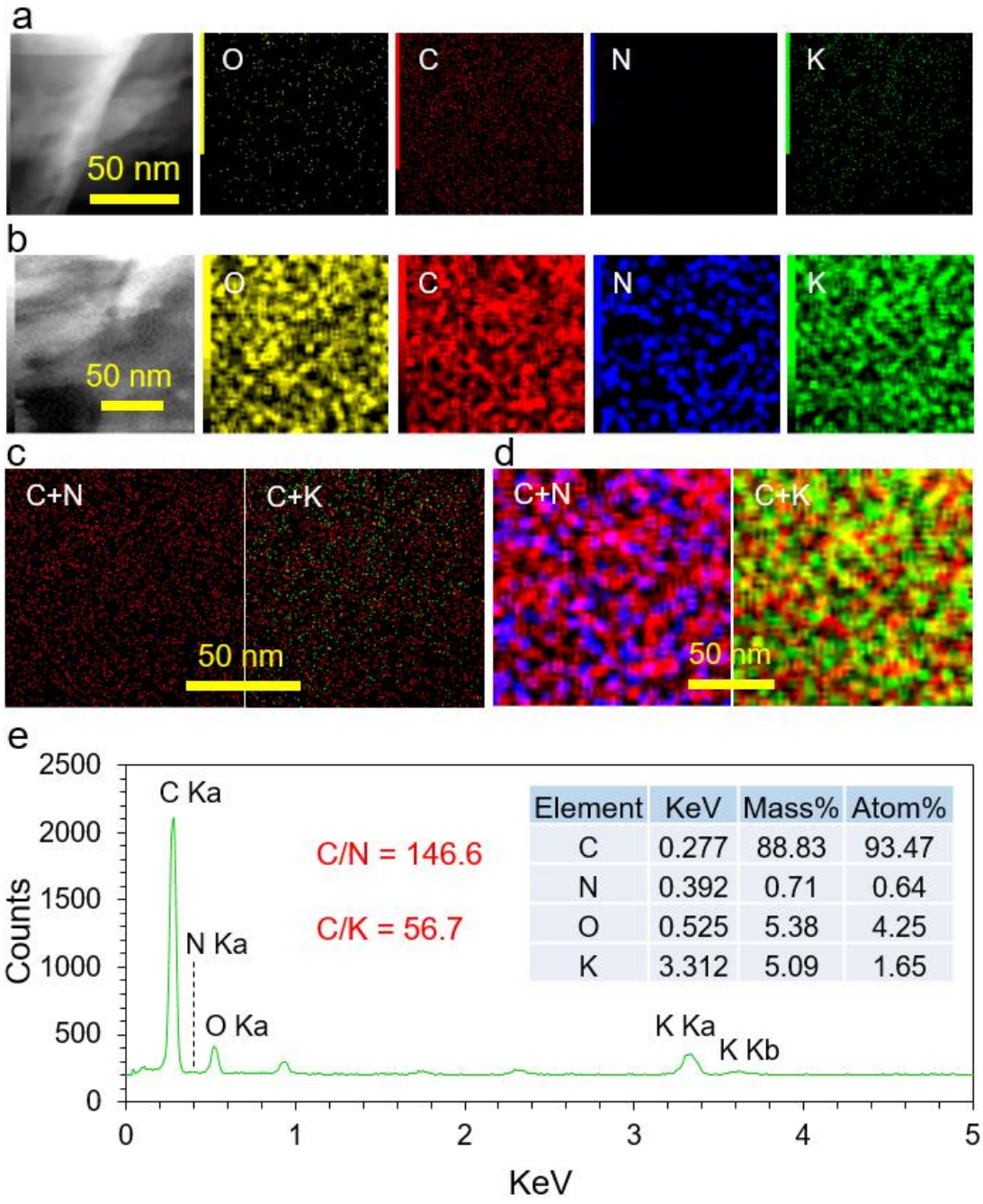

Supplementary Fig. 10 | Energy dispersive spectrum (EDS) analysis on the Stage-II K-NGF sample. a, b, Two kinds of EDS mapping images for the possible elements in the sample. **c, d,** Composite EDS mapping images for C and N elements as well as C and K elements based on the results in (**a, b**). **e,** EDS quantitative analysis results for the C, N, O, and K elements. The content of N element is very close to that detected in the fresh NGF sample (Supplementary Fig. 2). The rough mapping images should indicate all of the elements including the intercalated K atoms are evenly distributed.

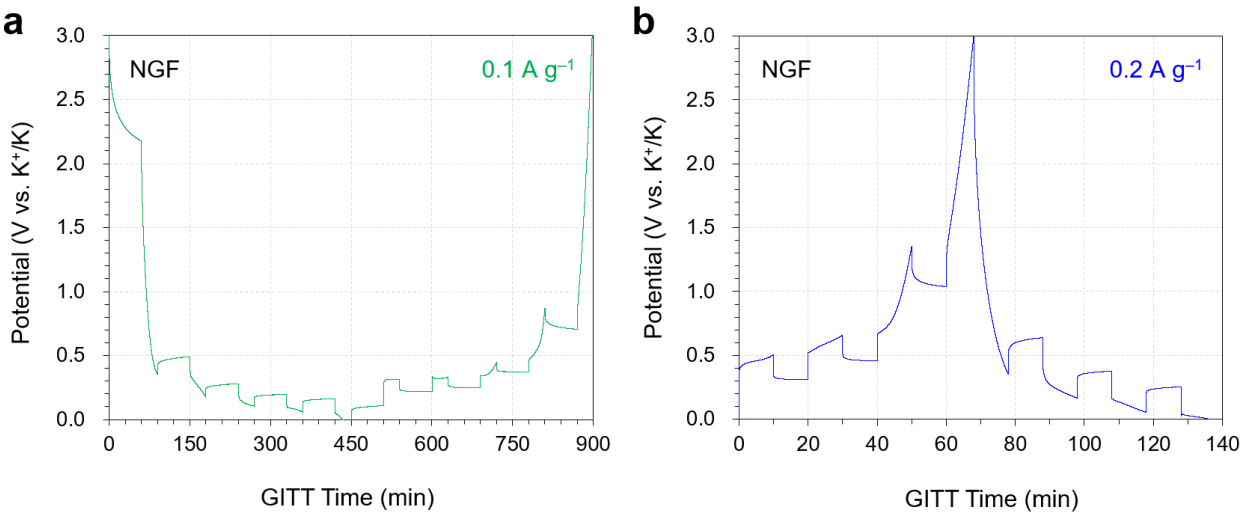

Supplementary Fig. 11 | Raw GITT profiles of the NGF electrode at different discharge-charge modes. a, At a current pulse of 0.1 A g^{-1} for 60 min alternated with a 30 min-OCP period to reach quasi-equilibrium potential. **b,** At a current pulse of 0.2 A g^{-1} for 10 min alternated with a 10 min-OCP period to reach quasi-equilibrium potential. The D_k values were calculated according to the widely reported method as shown in refs. 4–6.

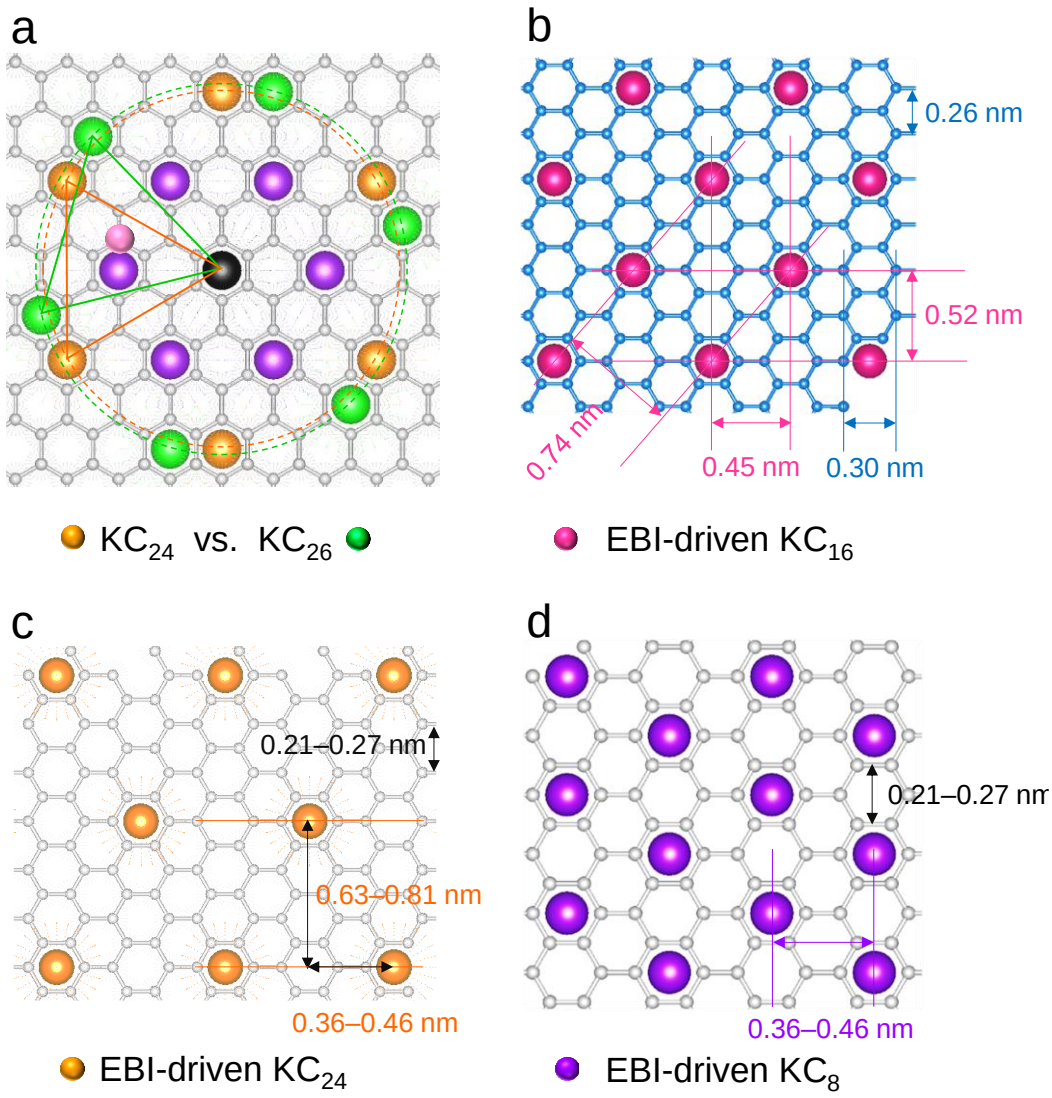

Supplementary Fig. 12 | Planar structure models for related KC_x phases. a, Planar distribution of K atoms for KC_{24} versus KC_{26}. **b,** Possible KC_{16} structure induced by the EBI effect. This is not the intrinsic structure of KC_{16} under electrochemical conditions but a supposed local structure derived from KC_{24} in view of the HR-TEM image analysis in Supplementary Figs 15–20. The strong EBI would drive a bunch of K atoms to move regularly in the graphene interlayers of KC_x and thus change the original distribution of K atoms in the electrochemical product. **c, d,** Possible crystal lattice spacings of the KC_{24} and KC_8 phases under the EBI. Driven by the EBI effect, the C atom-constructed lattices would expand by some extent due to the squeeze from the interlayered K atoms (refer to more structure parameters in ref. 1). When this happens, the K atom-constructed lattices would emerge in the HR-TEM images and SAED patterns (refer to the following TEM-based Characterization results).

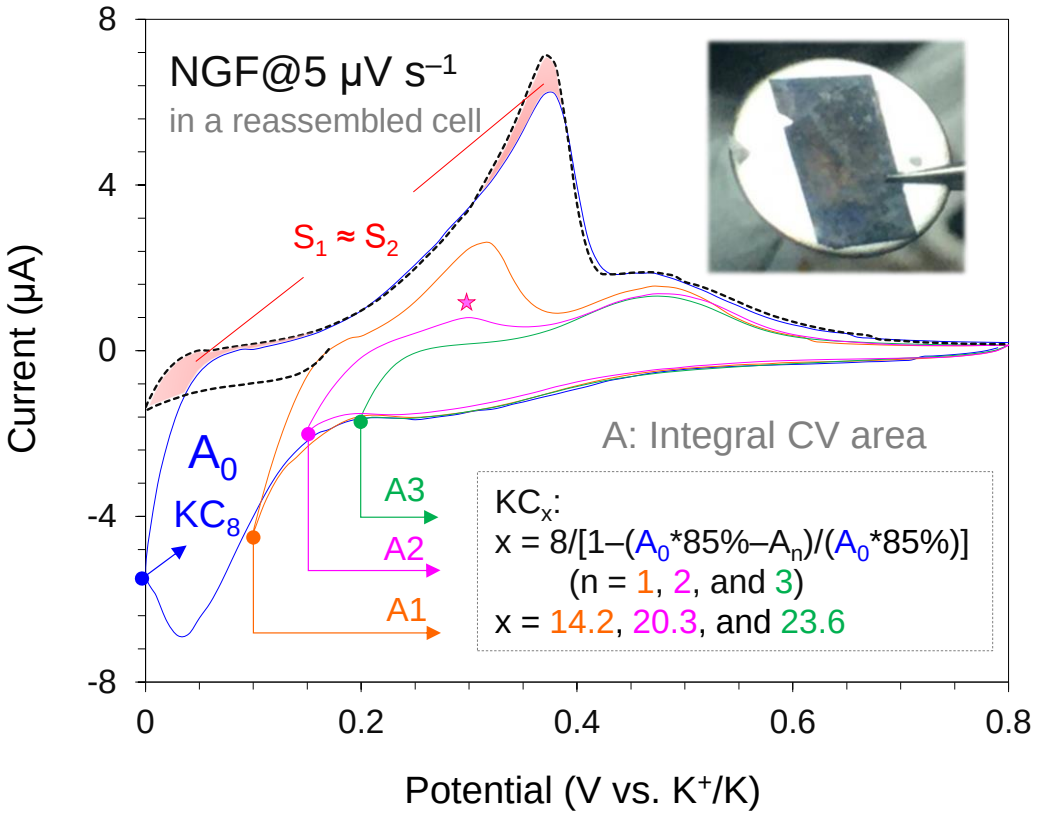

Supplementary Fig. 13 | CV curves with varied potential windows of the 2# NGF sample at 5 μV s^{-1} in a reassembled K-ion cell using 1 M potassium hexafluorophosphate (KPF_6) dissolved in the mixture of EC (ethylene carbonate), DEC (dimethyl carbonate), and EMC (ethyl methyl carbonate) as electrolyte. The KC_x composition at each cut-off potential such as 0.10, 0.15, and 0.20 V was calculated according to the area ratios of the whole CV curves as marked in the figure, where the defect contribution was also excluded here (ca. 15% as discussed in Fig. 2). In line with the resulted general KC_x formulars and the corresponding potentials, the pure KC_{24} product should be generated between 0.15 V and 0.20 V at this case, too. This result is similar to that using the initial KTFSI electrolyte despite of the different CV shapes in the two cases.

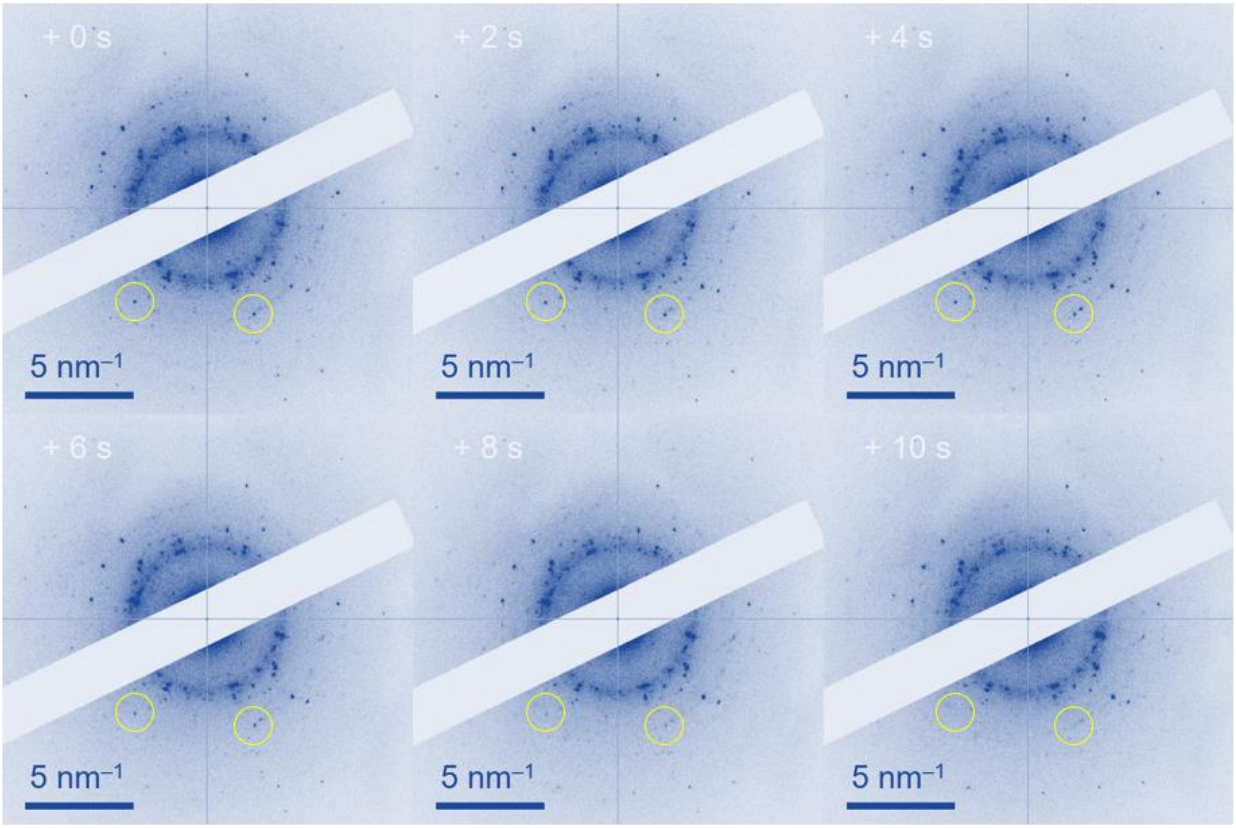

Supplementary Fig. 14 | SAED patterns captured continuously from a same region of the Stage-II K-NGF material. The fast but regular variations of the characteristic diffraction spots (refer to the remarked ones in the images) reflect the structure change of the material under the electron-beam irradiation (EBI). To see the EBI-caused variation more clearly, please refer to the GIF profile made up of these images show in Supplementary Video 1 as well as Fig. 4d**.** Knowing the unavoidable physical interference of EBI on the structure of the potassiated sample, as well as its SAED patterns or HR-TEM images, can greatly help ascertain its intrinsic/real configuration by backward reasoning[1]. Generally, the emerging multiple pairs of diffraction spots, some of which tend to form a ring, should imply the coexistence of the intrinsic and EBI-induced expanded graphene lattices.

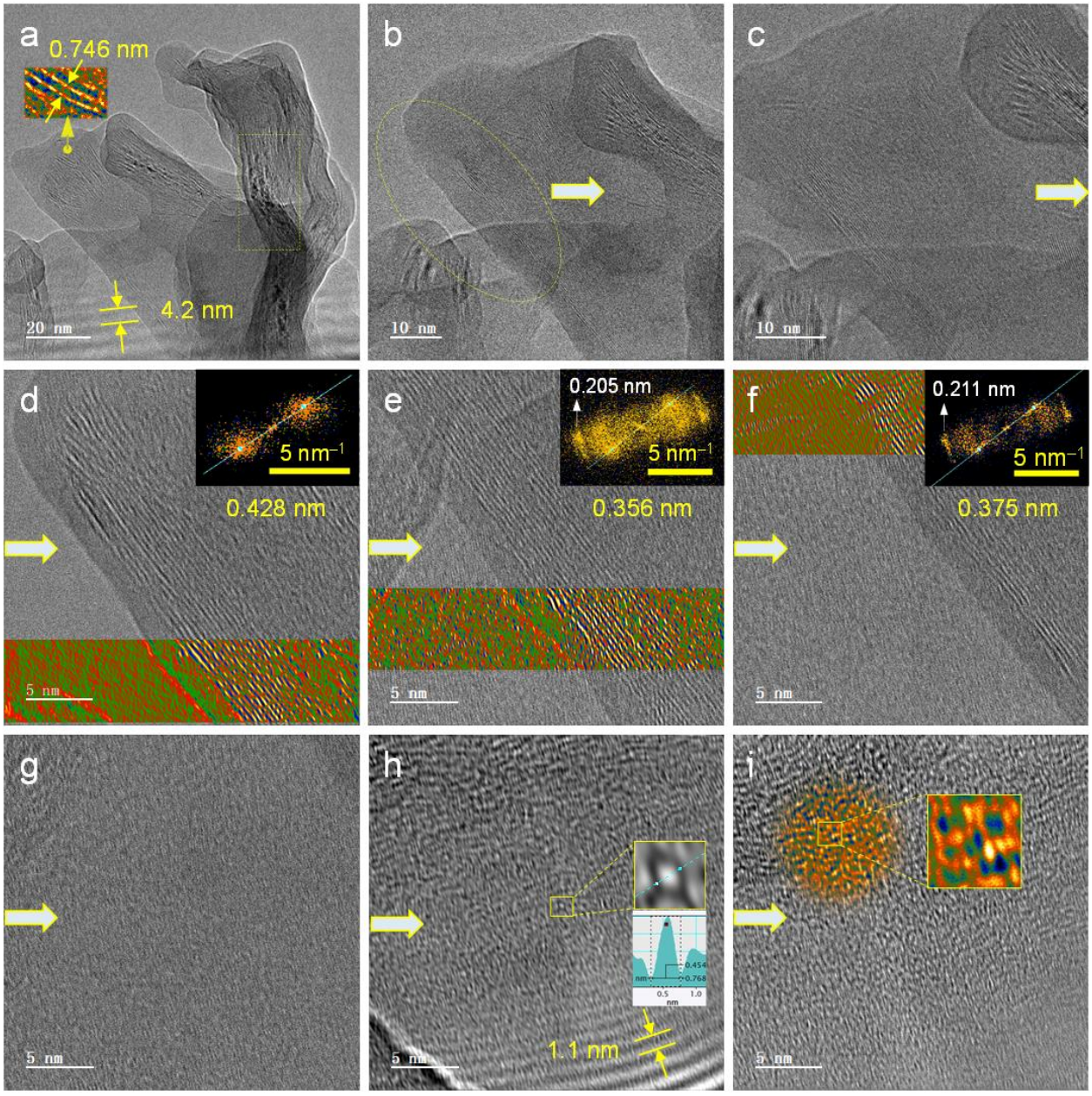

Supplementary Fig. 15 | HR-TEM images captured continuously from a same region of the Stage-II K-NGF material. a, Panoramic image captured at the very beginning for the following HR-TEM images shown in (**b**–**i**). **b**–**i,** HR-TEM images captured quickly as the field of view continuously drifted under EBI (with the accelerating voltage at 200 kV). The basal plane of the graphene sheet (**a**) clearly shows lattice fringes with very large interplanar spacing (which disappeared soon), ca. 0.75 nm as shown in the enlarged inset, which probably correspond to the plane of the K intercalant layers (Supplementary Fig. 12b, c). The decreased spacing for the lattice planes at the marginal area (**d–f**) present the similar phenomena caused by EBI. In addition, wavy fringes are often observed at the plane areas (**a, h**), which should be caused by the movements of vast of K atoms (refer to the insets of (**h, i**)).

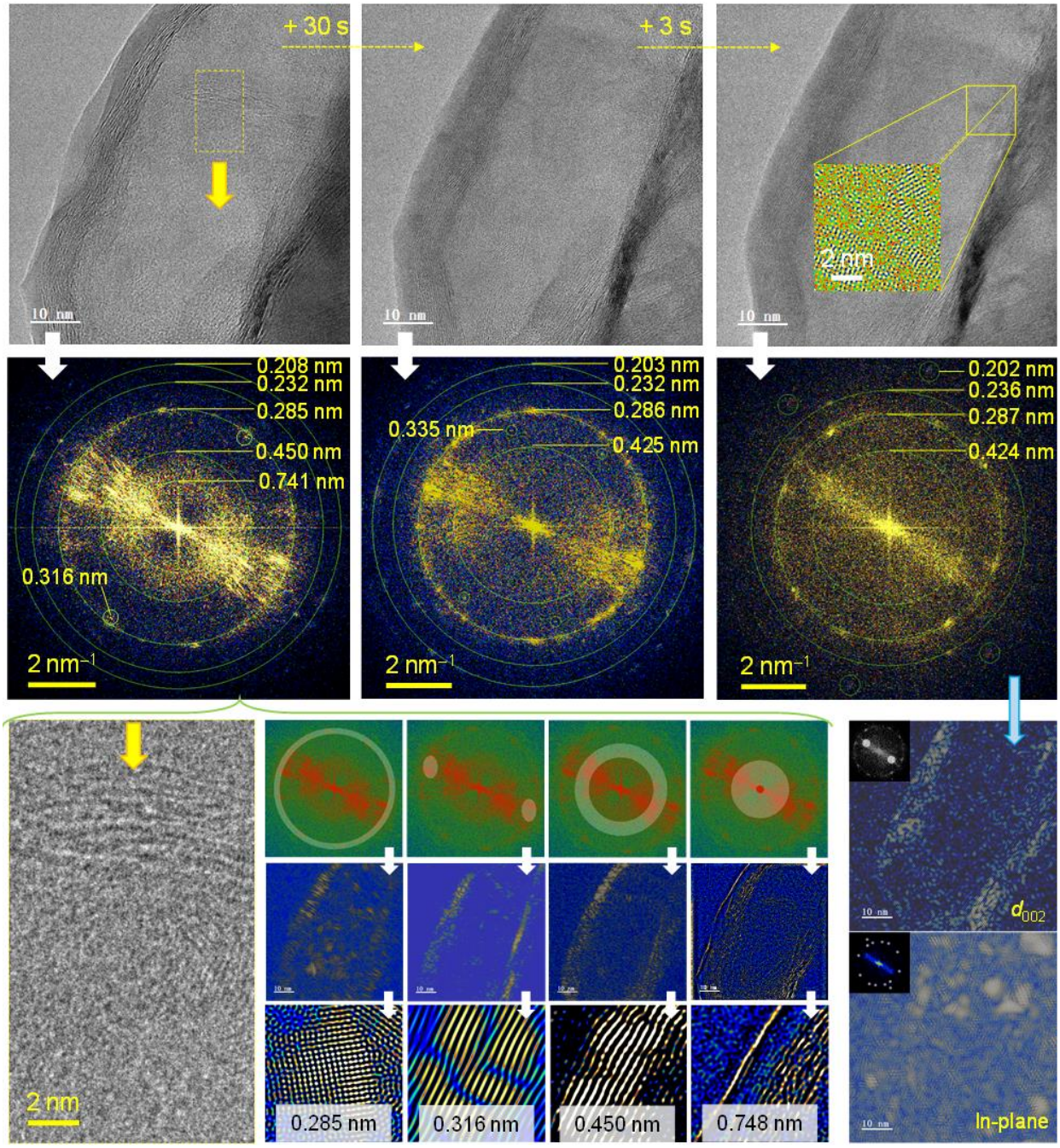

Supplementary Fig. 16 | Continuously captured HR-TEM images from a marginal region of the Stage-II K-NGF material, as well as their FFT patterns and inverse FFT images for specific planes with different lattice spacings. The regular image evolution further illustrates the strong EBI effect on the structure of the potassiated sample, in agreement with the phenomena reflected by Supplementary Fig. 15 and the following Supplementary Fig. 17a–d.

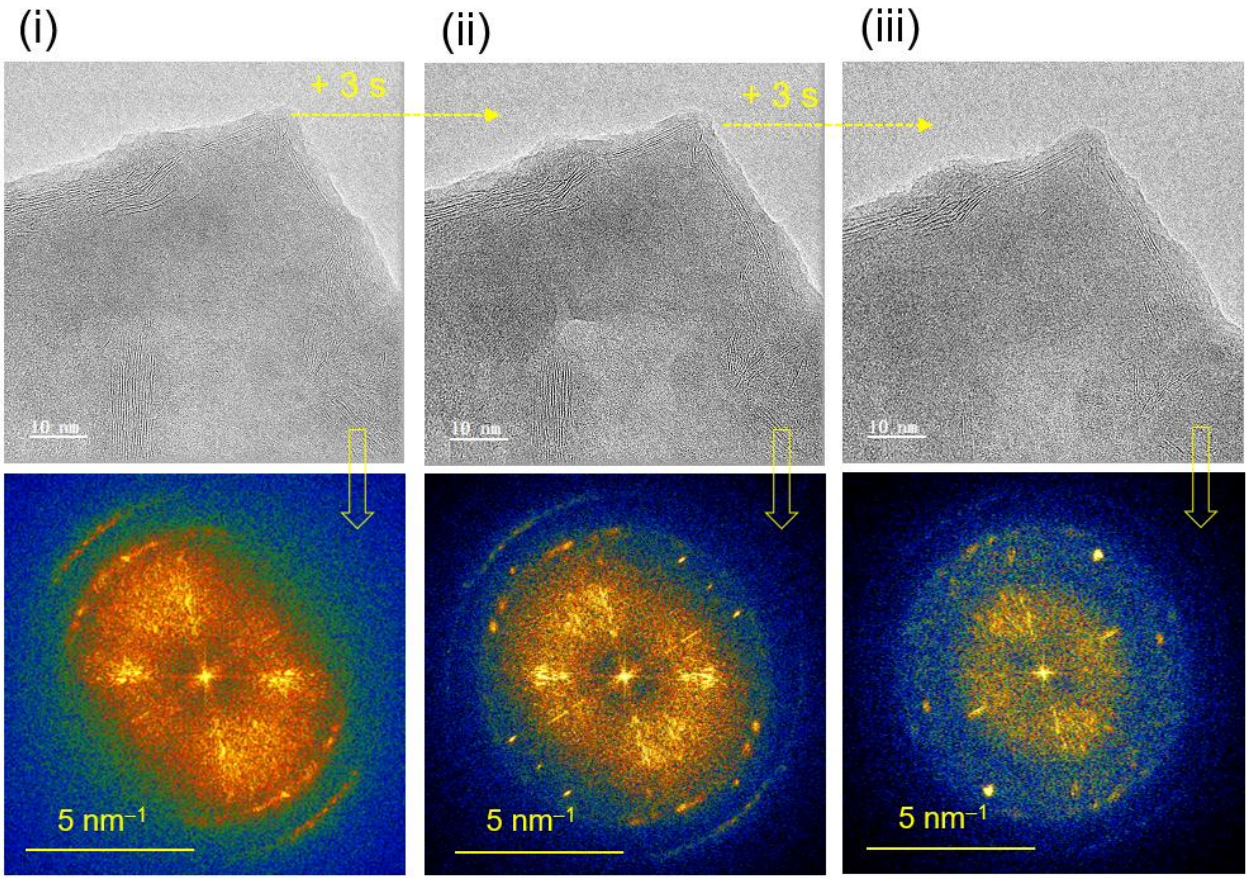

Supplementary Fig. 17a | Continuously captured HR-TEM images from a corner region of the Stage-II K-NGF material, as well as their FFT patterns. The EBI causes great structural changes in the region as well, for which the detailed analysis and comparison are shown in Supplementary Fig. 17b–d. It is worth mentioning that, although the images (namely the structure or lattice parameters) of the potassiated sample are changing all the time, they can be reasonably analyzed and explained in view of the collaborative influences from the initial interplanar spacing affected by N doping, the amount of K atoms embedded between the graphene interlayer, the real-time EBI intensity, and so on.

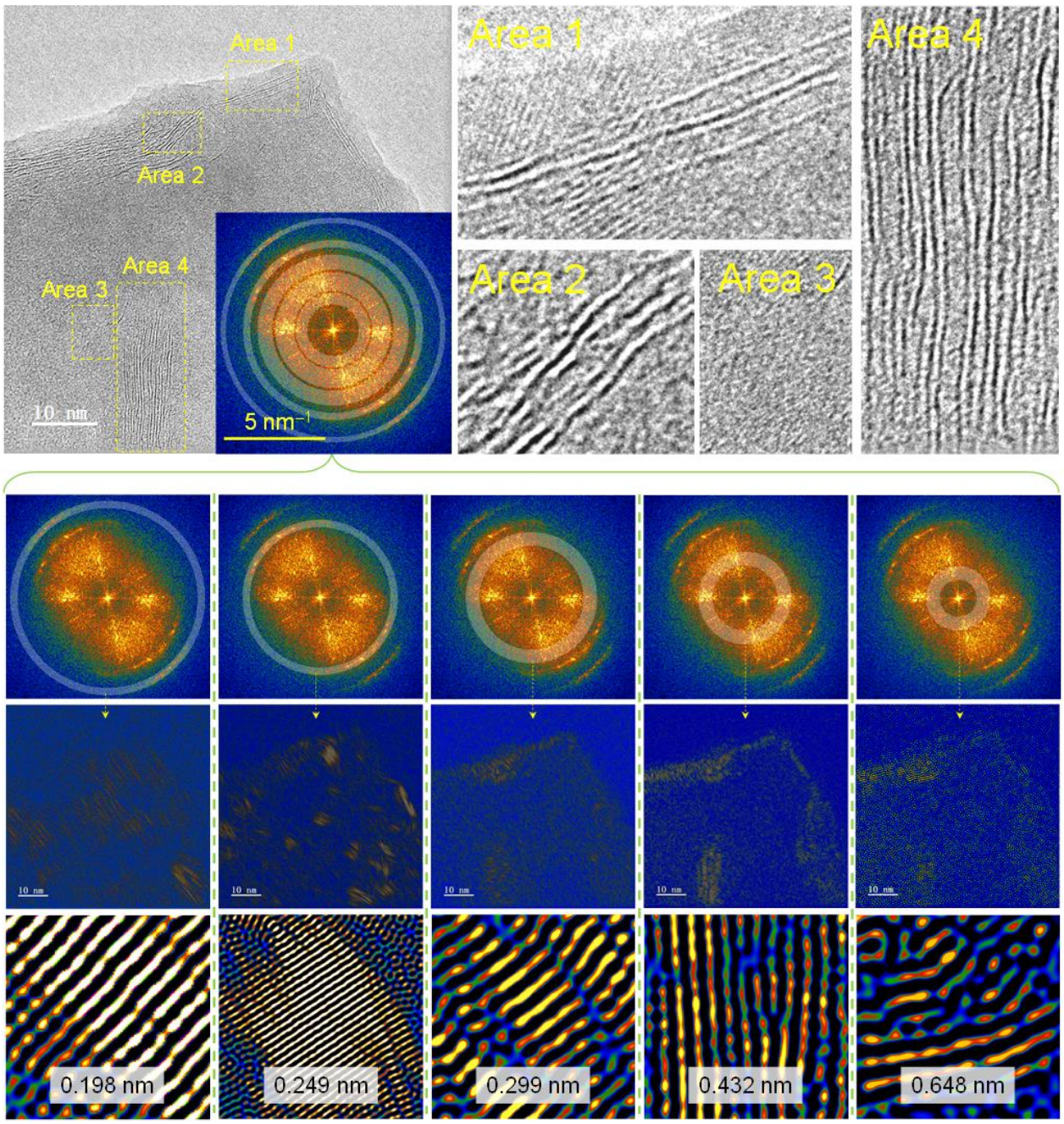

Supplementary Fig. 17b | Structure analysis for the Stage-II K-NGF material under EBI based on the image in Supplementary Fig. 17a(i). Four areas are chosen as the reference, as marked in the raw HR-TEM image and enlarged beside it (the first row). Meanwhile, the mask tool (see the FFT patterns at the second row) is used to identify and label the distribution of crystal faces with different lattice spacings (refer to the bright area in each inverse-FFT image at the third row). Thus, it is possible to find the typical crystal faces assigned to the indistinct diffraction spots distributing in different areas and then to obtain/measure the main lattice spacings (refer to the high-resolution images at the fourth row).

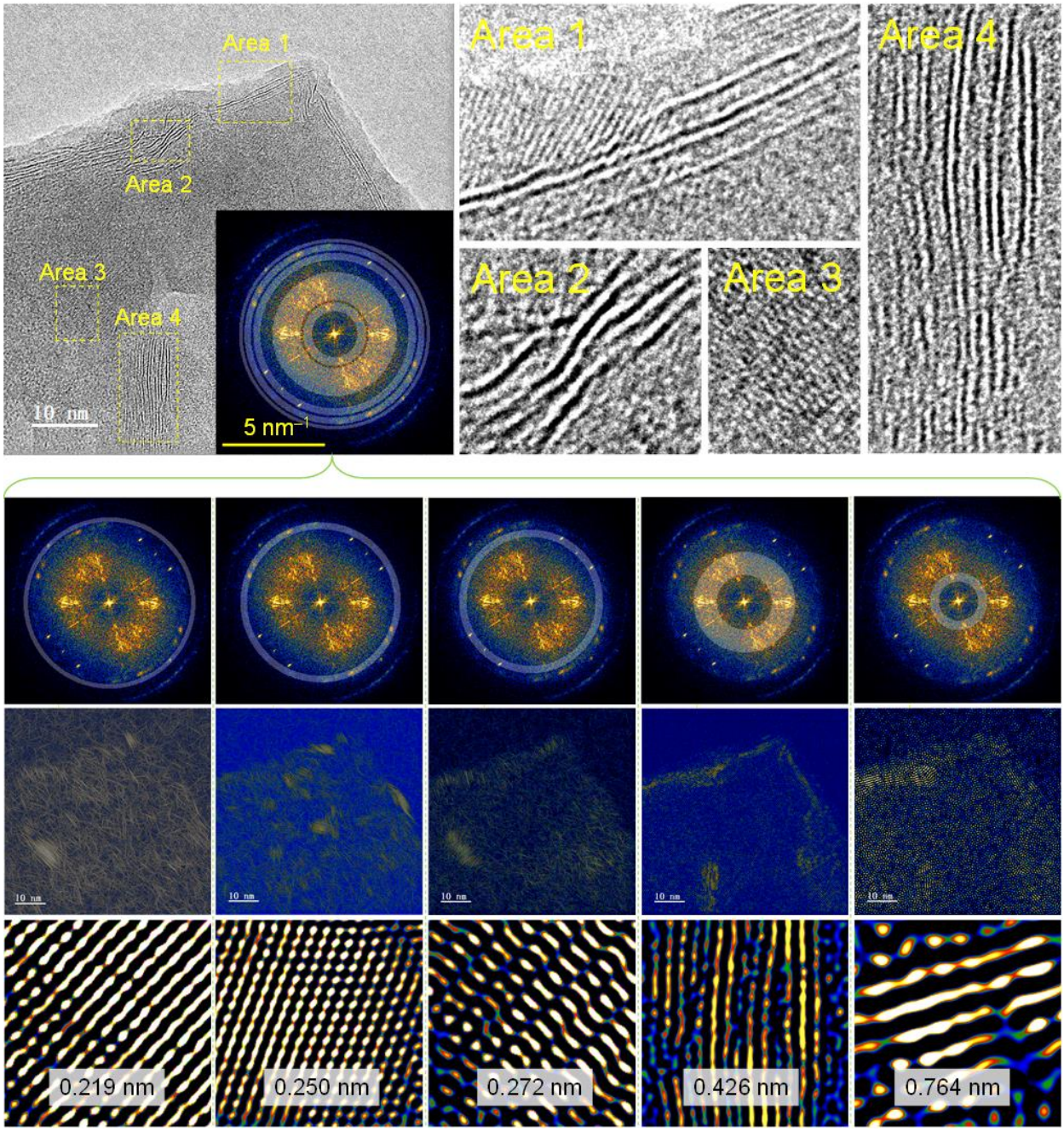

Supplementary Fig. 17c | Structure analysis for the Stage-II K-NGF material under EBI based on the image in Supplementary Fig. 17a(ii). Obviously, there was a noticeable change in the crystal structure of the potassiated NGF sample exposed in the EBI for a longer time.

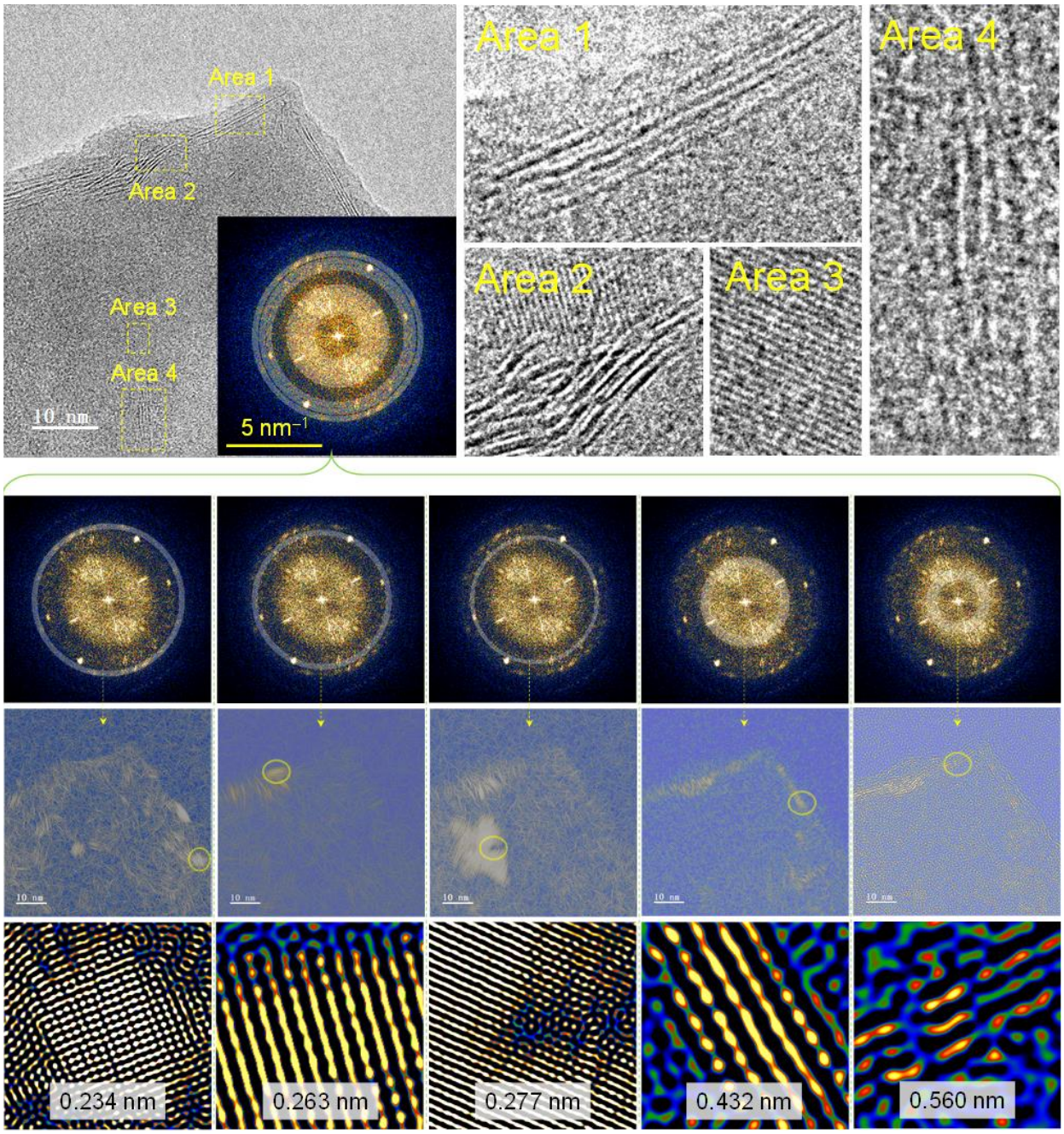

Supplementary Fig. 17d | Structure analysis for the Stage-II K-NGF material under EBI based on the image in Supplementary Fig. 17a(iii). After enough long-time EBI, both of the C-related and K-related crystal lattices would stabilize (at a state deviating from the standard)[1].

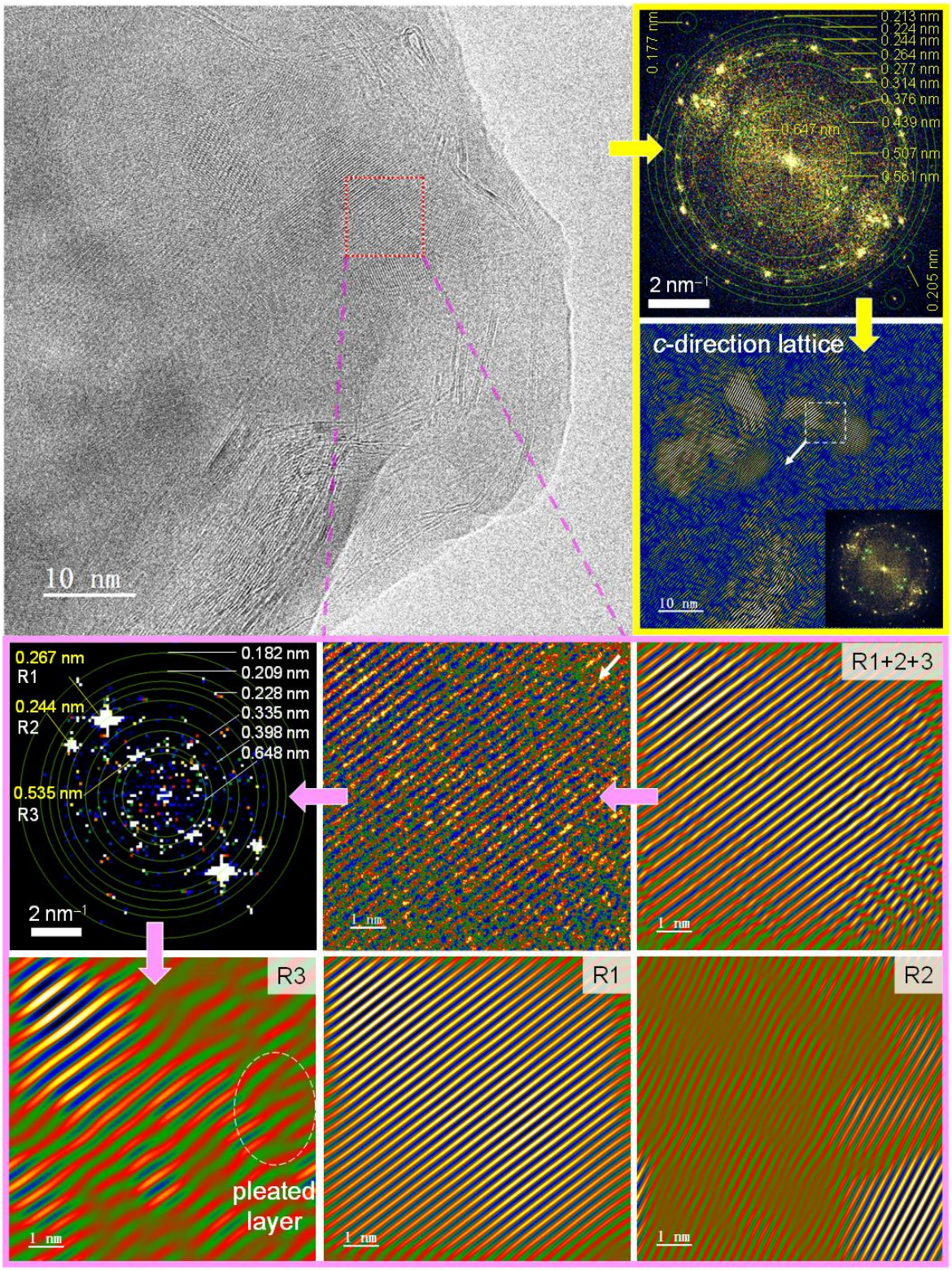

Supplementary Fig. 18 | HR-TEM image from a thick region of the Stage-II K-NGF material and the FFT-assisted structure analysis. Here different lattice faces in particular the (002) planes were distinguished for a local region (as marked in the HR-TEM image) based on its FFT pattern.

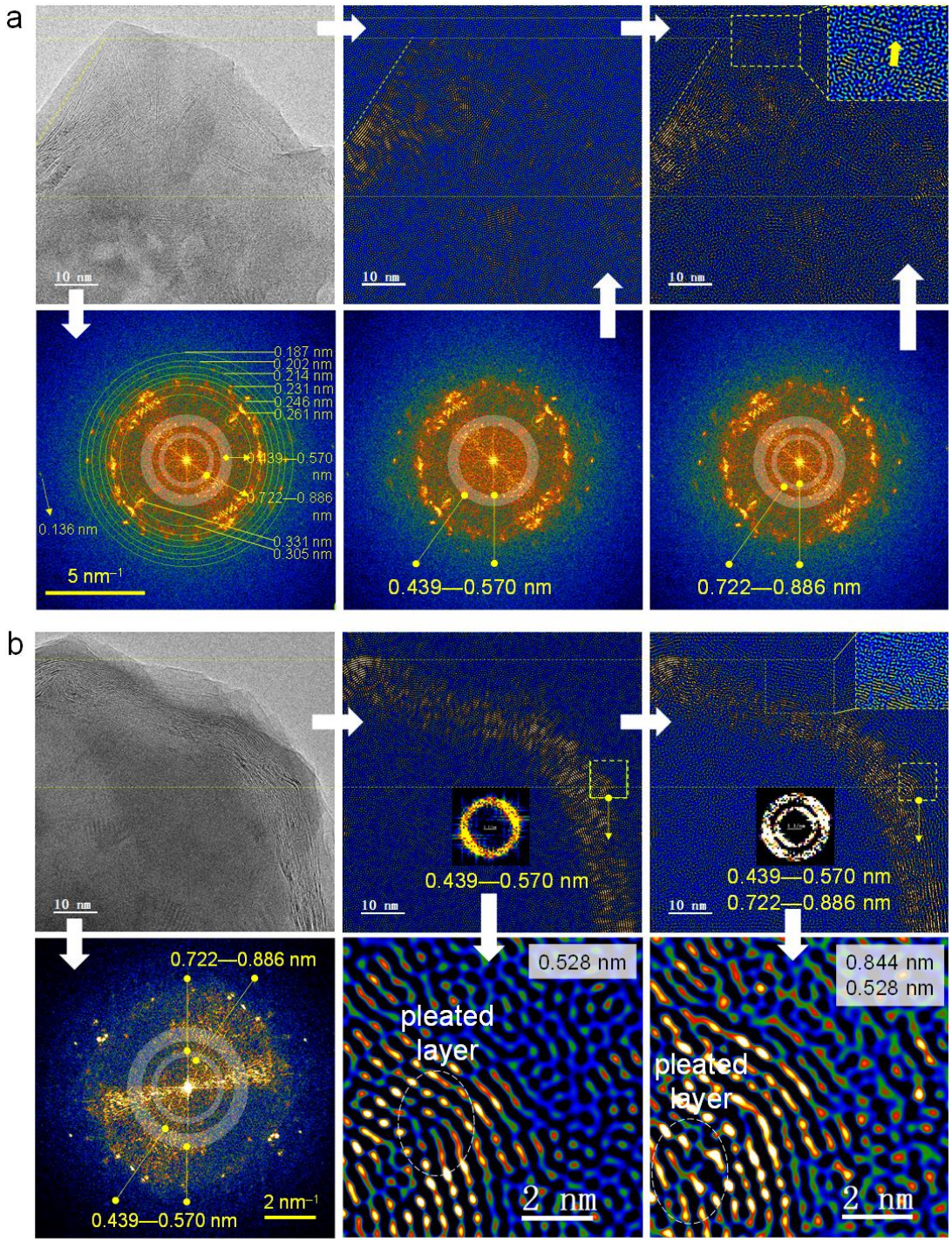

Supplementary Fig. 19 | FFT-assisted positioning for (002) crystal faces of the K-NGF material. a, HR-TEM image of a marginal area. **b,** HR-TEM image of a corner region. Here inverse FFT images representing specified lattice sizes were obtained by apply suitable ring-shape masks to the HR-TEM images-derived FFT pattens. Judging from the locations of the crystal faces with spacing sizes at 0.44–0.57 nm (close to the d_{002} values of KC_{24} and KC_8) and their width (~10 nm), it is reasonable to assign these regions to the (002) planes of the K-NGF electrode under EBI. Some pleated-layer defects are also observed here, which can further support this inference.

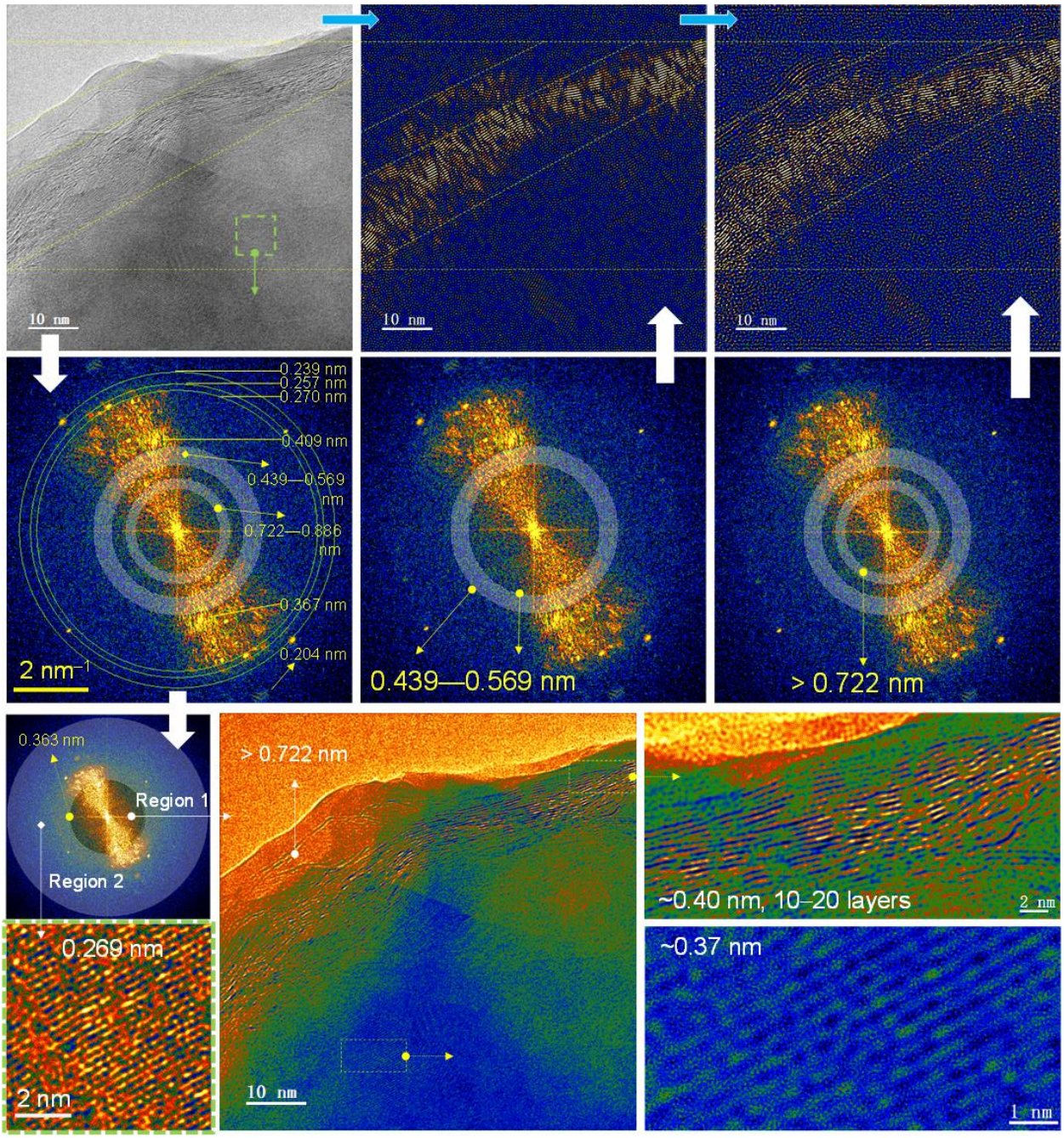

Supplementary Fig. 20 | FFT-assisted positioning for (002) crystal planes of the potassiated NGF electrode under EBI. In view of the EBI effect (Fig. 4b**)** and the possible lattice spacings of the potassiated graphite material under EBI (see Supplementary Fig. 12 and ref. 1), the (002) planes of the Stage-II K-NGF electrode can be determined to locate at the marginal area by applying the FFT-mask process method illustrated in Supplementary Figs 15–19. Thus, judging from the colored HR-TEM image at the bottom exhibiting only crystal faces with lattice spacing > 0.36 nm (corresponding to Region 1 in the FFT pattern), the (002) planes with or without K atom intercalation are always uniform in the lattice spacing. Such a scene obviously goes against the two widely used historical models and thus exemplifies their irrationality.

Supplementary Video

Supplementary Video 1. An *in-situ* SAED video showing the EBI-driven changes of SAED patterns for the Stage-II K-NGF electrode (Supplementary Fig. 14).

References

[1] Ji, K. M. et al. Lithium intercalation into bilayer graphene. *Nat. Commun.* **10**, 275 (2019).

[2] Conway, B. E. *Electrochemical supercapacitors – Scientific fundamentals and technological applications*. Kluwer Academic/Plenum Publishers, New York (1999).

[3] Jian, Z. L., Luo, W. & Ji, X. L. Carbon electrodes for K-ion batteries. *J. Am. Chem. Soc.* **137**, 11566−11569 (2015).

[4] Liu, J. L. et al. Unraveling the potassium storage mechanism in graphite foam. *Adv. Energy Mater.* **9**, 1900579 (2019).

[5] Xu, Y. et al. Highly nitrogen doped carbon nanofibers with superior rate capability and cyclability for potassium ion batteries. *Nat. Commun.* **9**, 1720 (2018).

[6] Zeng, S. F. et al. Boosting the potassium storage performance of carbon anode via integration of adsorption-intercalation hybrid mechanisms. *Nano Energy* **73**, 104807 (2020).